NANO LETTERS

pubs.acs.org/NanoLett

Letter

Full-Space and Arbitrary Orbital Angular Momentum Multiplexed Beam Manipulation with a Titanium Dioxide Metadevice

Wei Zhu, Yuancheng Fan,* Ruisheng Yang, Huan Zhao, Guangzhou Geng, Xuyue Guo, Peng Li, Quanhong Fu, Kangyao Sun, Changzhi Gu, Yan Zhang, Junjie Li,* and Fuli Zhang*

Cite This: *Nano Lett.* 2025, 25, 14237−14245

Read Online

ACCESS | Metrics & More | Article Recommendations | Supporting Information

ABSTRACT: A titanium oxide (TiO_2) metasurface is emerging as a promising platform for arbitrary control of visible light and has been demonstrated for metalenses, a helicity multiplexed hologram, chiral spectroscopy, and structural colors. Among these, the generated orbital angular momentum (OAM) beam endows additional freedom in complex light−matter interactions. Manipulating multiple OAM channels within a single metadevice is highly coveted, and such capability proves advantageous for the advancement of integrated photonic chips and the creation of miniaturized optical systems tailored for applications involving OAM light. Here, an all-dielectric metasurface made of spatially rotated TiO_2 nanofins is demonstrated experimentally for the generation, spatial multiplexing, and focusing of the OAM light in both angular and distance domains. In particular, our metadevice could reconstruct four different topologically charged beams into four different directions and focus in four different planes in a broadband manner. The ultracompact spatially multiplexing on-chip metadevice may inspire exterior photonic applications with versatile integrated functionalities.

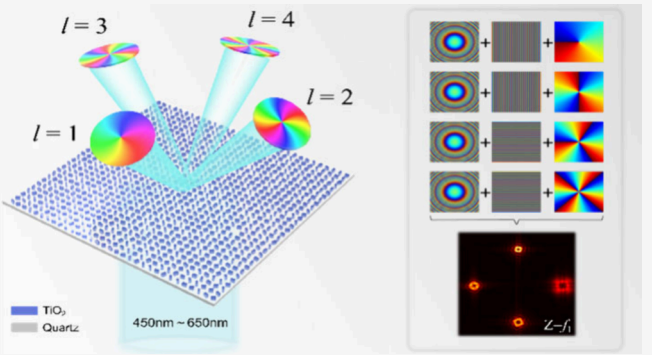

KEYWORDS: *orbital angular momentum, spatial multiplexing, all-dielectric metasurface, titanium dioxide*

The titanium dioxide (TiO_2) metasurface is emerging as a promising platform for the high-performance integrated photonic device to arbitrarily manipulate light by exploiting its high refractive index and ultralow optical loss across the visible spectrum.[1,2] Recently, TiO_2 metasurfaces have shown great capability for arbitrarily controlling the wavefront within the entire visible spectrum and have inspired various light manipulations with exotic functionalities including metalenses,[3] a helicity multiplexed hologram,[4] beam steering,[5] chiral spectroscopy,[6] structural colors,[7] and spin-orbital conversion.[8] Such advantages can also be extended for the generation of an orbital angular momentum (OAM) beam with additional freedom in complex light−matter interactions.[9,10]

OAM of light, with an azimuthal phase gradient, has been an enticing topic for both theoretical and applied researches over the last couple of decades since optical phase singularities were discovered by Allen et al. in 1992.[11] These phase singularities are a key feature of optical vortices (OVs), which manifest as beams carrying OAM.[10] An OV is characterized by a dark core with zero intensity along the beam axis, surrounded by an annular transverse intensity profile.[12] While OVs are typically associated with beams carrying the OAM, another distinct property of light is spin angular momentum (SAM), representing the spin state of photons. Unlike the discrete SAM, the OAM can assume continuous values, including both integer and noninteger states. Phase singularity is the distinguishing feature of OVs, which indicates a dark core with zero intensity along the beam axis together with an annular transverse intensity profile.[12] OVs usually refer to a beam-carrying OAM.[10] SAM is another property of light that represents the spin state of a photon. Unlike SAM, the OAM can take any value in a continuous range, either integer or noninteger. Therefore, the unbounded OAM states can provide additional data transmission channels and impact many branches of optical applications including optical tweezers and spanners,[13] quantum information encoding,[14,15] nonlinear optics,[16] and high-speed communications.[17,18] However, traditional devices for generating OVs, including spatial light modulators,[19] Q plates,[20] spiral phase plates,[21,22] and computer-generated holograms,[23,24] are still limited to their compatibility with a miniaturized optical system and cannot be easily embedded into integrated photonic chips.

Received: May 8, 2025
Revised: September 9, 2025
Accepted: September 11, 2025
Published: September 22, 2025

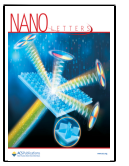

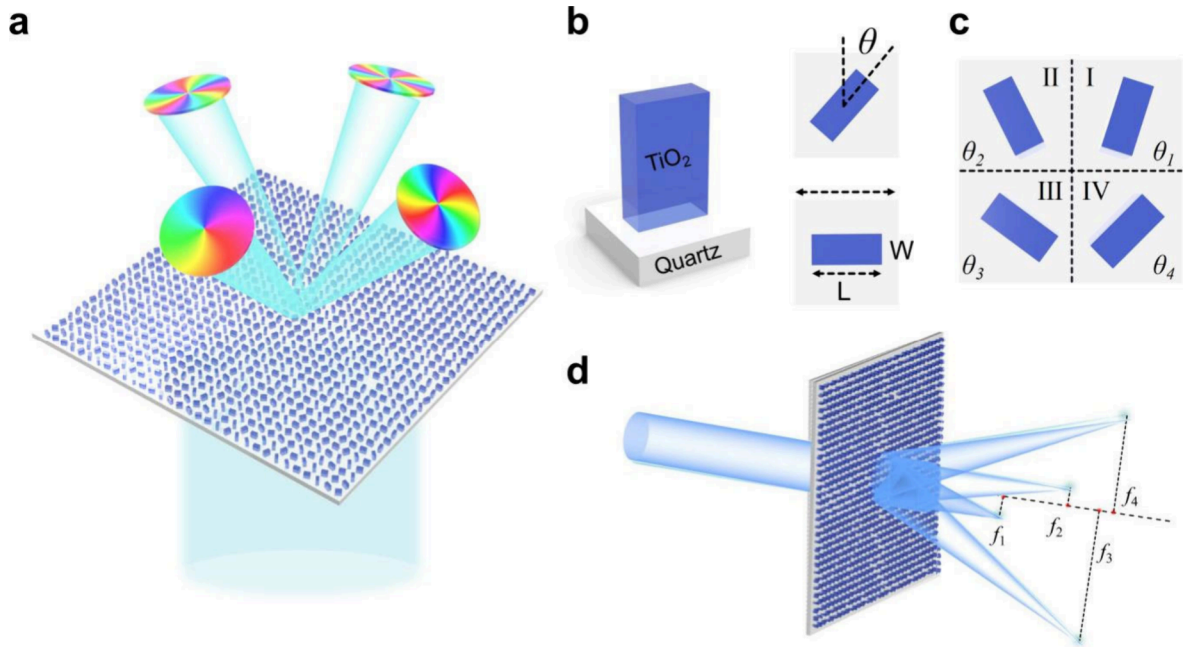

Figure 1. Schematic of the SMM. (a) Schematic illustration of the working mechanism of the metasurface. (b) Side and top views of the nanofin. Top views of a nanofin showing width W, length L with individual dimensions $S \times S$, and rotation of the nanofin by an angle θ resulting in the required phase (geometric PB phase). Side view of a TiO_2 nanofin on a quartz substrate showing height H. Incident plane waves propagate along the z direction. The geometric parameters are S = 400 nm, W = 100 nm, L = 280 nm, and H = 600 nm. (c) Schematic diagram of the unit cell, which enables independent manipulation of the four different output beams. (d) Four output beams that obtain different focal lengths along the z-axis direction.

To address these limitations, recent advances in metasurface technology have shown great potential, beginning with the demonstration of OV beams via a metasurface composed of V-shaped nanorods by Yu et al. in 2011.[25] At the same time, the interferometric approach was proposed to extract the spiral phasefronts of the scattered vortex beam. To make the OAM operation of light more efficient and flexible, the Pancharatnam−Berry (PB) phase was introduced, which controls the phase of the scattered light by spatially rotating each subwavelength unit cell (Figure S1). The metasurface carrying the PB phase enables a continuous phase change, which arises from the double relationship between the transmission phase and the nanostructure orientation angle. This allows a more accurate reconstruction of the wavefront.[26,27] Related research based on plasmonic metasurfaces to modulate OAM has been widely reported.[28,29] However, high ohmic losses arising from plasmonic metasurfaces are difficult to overcome, especially in visible frequencies.[30] To avoid the ohmic damping produced by the metal, all-dielectric metasurfaces with building blocks of high-refractive and low-loss dielectrics[31−33] have recently been proposed as an alternative route to realize the high-efficiency manipulation of OAM.[34−37] Although vortex beams generated by all-dielectric metasurfaces have been extensively studied, recent advances in structured light manipulation have revolutionized polarization and vortex multiplexing across diverse applications. Pioneering works have demonstrated far-field multiplexed vortex generation[38] and near-field OAM coupling in dielectric platforms,[39] while breakthroughs in single-shot isotropic microscopy[40] and material-engineered photonic devices[41] highlight the expanding applications of OAM multiplexing. Our work establishes a unified framework that bridges these domains, achieving full-space OAM manipulation in miniaturized systems with performance metrics surpassing those of current imaging approaches while maintaining compatibility with next-generation integrated photonics.

Here, we have proposed and experimentally demonstrated a TiO_2-based metadevice for spatially multiplexing the OAM manipulation in both angular and distance domains. By spatially rotating TiO_2 nanofins to control the geometric phase of spin light, the metadevice can achieve generation, spatial multiplexing, and focusing of the OAM light at visible wavelength. After a plane wave passes through the metadevice, a plane wave can be divided into four different topologically charged beams into four different directions and focus in four different planes in a broadband manner. Our spatial multiplexing metadevice (SMM) takes advantage of full-space manipulation and arbitrary multiplexing of OAM beams, which is beneficial for ultracompact photonic devices with more unique extensibility and flexibility in versatile optical elements than traditional phase-accumulated helical optical devices.

To realize the spatially multiplexing function, the designed metadevice consists of spatial-variant TiO_2 nanofins capable of dividing the incident circular polarization (CP) light into four different topologically charged beams into four different directions and focusing in four different planes, as shown in Figure 1a. The building blocks of our metadevice are high-aspect-ratio TiO_2 nanofins standing on a quartz substrate, as shown in Figure 1b. Each TiO_2 nanofin acts as a half-wave plate due to the high-efficiency cross-polarization derived from the π-phase delay between the long and short axes of a nanofin. The required phase is imparted by rotation of the nanofin by an angle θ based on the PB phase resulting from space-variant polarization manipulation instead of the optical path difference.

It is easy to observe from Figure 1c that the unit cell of the SMM has four rotation-variant nanofins, each coded into different subareas. The in-plane lateral dimensions of the

https://doi.org/10.1021/acs.nanolett.5c02519
Nano Lett. 2025, 25, 14237−14245

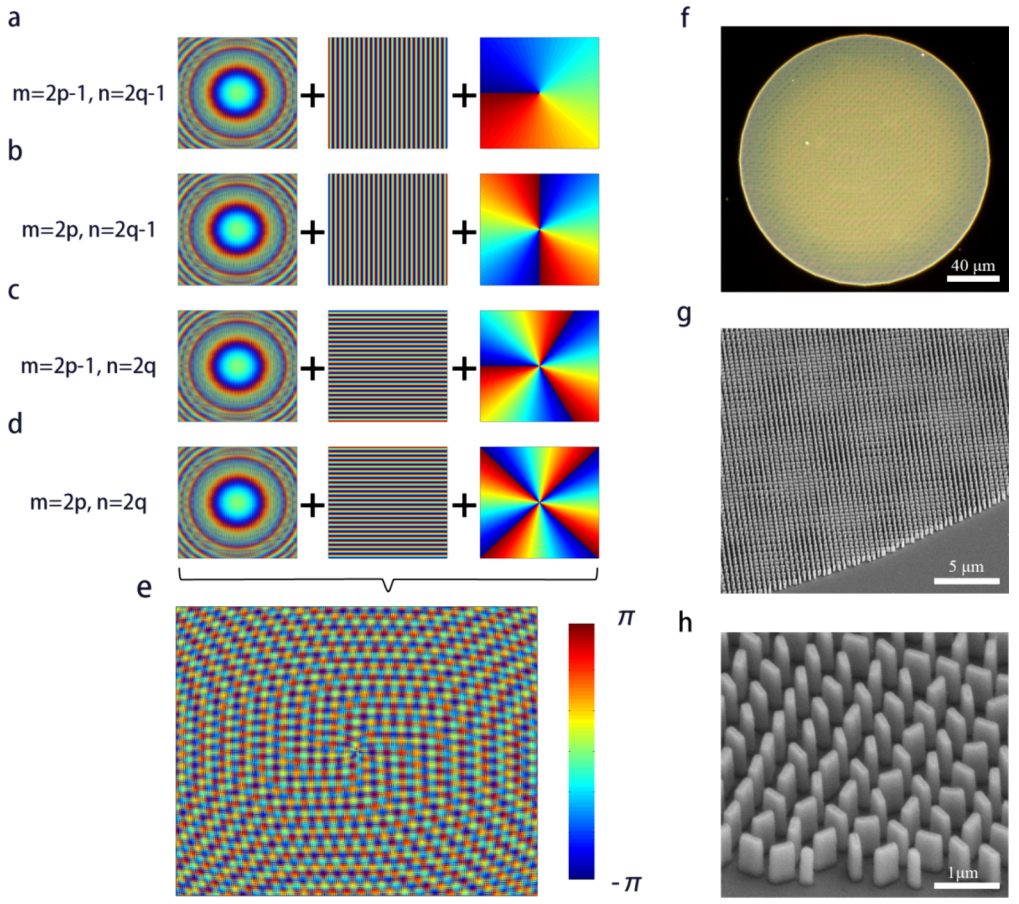

Figure 2. Design and fabrication of the SMM by utilizing the space-variant geometrical phase and SEM images of the sample. (a–d) Illustration of how to obtain the composite phase profiles by merging three types of phases in different locations. (e) Complete superimposed phase profiles of the whole SMM sample, which consists of 400 × 400 unit cells. (f–h) Gradient-magnified SEM images of the sample. The scale bars have been marked.

nanofin perpendicular and parallel to the optical axis are respectively defined as L and W, which are optimized to achieve the ultrahigh efficiency of cross-polarization. While numerous alternative sizes are capable of achieving ultrahigh efficiency for narrow-band cross-polarization (Figure S2), only a select few optimized sizes can attain ultrahigh efficiency for broadband cross-polarization. The unit cell, divided into four subregions (I/II/III/IV), plays a key role in the SMM. However, we are supposed to verify the approximate condition before designing the SMM, which enables simplification of the process of design. Figure 1d shows the 2D side view of the proposed SMM. The metadevice-generated focused OVs with topological charges of l = 1−4 corresponded to the tilt directions along the $+x$, $-x$, $+y$, and $-y$ axes, respectively. Moreover, the off-axis OVs have the capability of focusing on different focal planes with focal lengths that can be custom-designed, making them more flexible than other spatially multiplexing devices.

These unprecedented capabilities enable transformative applications across multiple domains: In optical tweezer systems, the simultaneous generation of multiple independently controlled vortex beams allows parallel trapping and 3D manipulation of particles at different spatial positions. For high-capacity optical communications, the four independent OAM channels serve as additional multiplexing dimensions that can be combined with wavelength-division multiplexing to significantly enhance the transmission capacity. In integrated photonic chips, the direct compatibility with semiconductor processes enables compact integration with lasers and detectors for the use of OAM-based quantum computing and information processing. These implementations are uniquely enabled by the device's spatial multiplexing capability, broadband operation, and CMOS compatibility, opening new technological pathways for complex optical field manipulation.

Due to the pure PB phase modulation method, the nanofins exhibit the same geometry but vary in the orientation angle θ. When circularly polarized (CP) light passes through them, the transmitted light switches to the opposite CP and undergoes an abrupt phase change of 2θ. In order to realize the multichannel OVs generator, the phase distributions of the electric field in the SMM plane (z = 0) are supposed to be calculated. To generate off-axis multiple OAM states, the complex electric field of the OAM beam with different phase shifts in the SMM plane can be acquired by linearly superimposing the individual complex field, which can be expressed as follows:

$$E(x, y, 0) = \sum_{m=1}^{p}\sum_{n=1}^{q} a_{mn}(x, y, 0) \times \exp\{-i[l_j\varphi(x, y) + \sigma_{\pm}k_0 \sin\theta_{jx}x + \sigma_{\pm}k_0 \sin\theta_{jy}y + \varphi_{j\_lens}(x, y)]\} \quad (1)$$

https://doi.org/10.1021/acs.nanolett.5c02519
Nano Lett. 2025, 25, 14237−14245

where m and n are the diffraction order in the x and y directions, $a_{mn}(x,y,0)$ is the amplitude distribution of individual OAM light, which determines the light intensity of the OAM light beams in the output plane, $\varphi(x,y) = \arctan(y/x)$ is the azimuthal angle, $k_0 = 2\pi/\lambda$ is the wavenumber in the free space, l_j is the topological charge of the corresponding vortex beam, and θ_{jx} and θ_{jy} are the propagation angles of light with respect to the x and y directions, respectively. The spin quantum numbers $\sigma_{\pm 1} = \pm 1$ represent the two orthogonal spin states $|\sigma_+\rangle = \begin{pmatrix} 1 \\ i \end{pmatrix}$ and $|\sigma_-\rangle = \begin{pmatrix} 1 \\ -i \end{pmatrix}$, denoting left-hand circular polarization (LCP) and right-hand circular polarization (RCP), respectively. $\varphi_{j\_\mathrm{lens}}(x,y)$ is the phase that enables determination of the focal length with different channels.

In this work, the number of OAM states $N = 4$ because the metadevice we proposed obtains four channels along the $+x$, $-x$, $+y$, and $-y$ axes. In general, the energy of each OV is equal because the duty cycle of each channel is the same. However, the energy of each OV has obvious differences, which is caused by the transmission loss and coupling of adjacent nanofins. Moreover, the phase distribution of the SMM could be obtained by the hologram principle and expressed as

$$\varphi(x, y) = \arg[E(x, y, 0)] \tag{2}$$

To achieve a multichannel and low cross-talk SMM, the unit cell is divided into subareas I–IV, each facilitating the provision of the required phase distribution for each channel independently. Thus, as depicted in Figure 2, the total phase distribution of the SMM is segmented into four parts and can be represented as

$$\varphi_{m,n}(x, y) = \begin{Bmatrix} \varphi_1(x, y), & m = 2p - 1, & n = 2q - 1 \\ \varphi_2(x, y), & m = 2p, & n = 2q - 1 \\ \varphi_3(x, y), & m = 2p - 1, & n = 2q \\ \varphi_4(x, y), & m = 2p, & n = 2q \end{Bmatrix} \quad p,\ q = 1,\ 2,\ 3,\ \ldots \tag{3}$$

where p and q are integers in the range of 1–200. In this way, the required phase profile in the nth row and the mth column of four areas corresponds to $\varphi_{m,n}(x,y)$, which consisted of a superposed phase, including the vortex phase with different values of topological charge l_j, the tilt phase, and the lens phase, that can be expressed as functions of the positions as follows:

$$\varphi_{m,n}(x, y) = \begin{Bmatrix} l_1 \arctan\left(\frac{y}{x}\right) + \frac{2\pi}{\lambda}\left(f_1 - \sqrt{x^2 + y^2 + f_1^2}\right) + \frac{2\pi}{\Lambda}x \\ l_2 \arctan\left(\frac{y}{x}\right) + \frac{2\pi}{\lambda}\left(f_2 - \sqrt{x^2 + y^2 + f_2^2}\right) - \frac{2\pi}{\Lambda}x \\ l_3 \arctan\left(\frac{y}{x}\right) + \frac{2\pi}{\lambda}\left(f_3 - \sqrt{x^2 + y^2 + f_3^2}\right) + \frac{2\pi}{\Lambda}y \\ l_4 \arctan\left(\frac{y}{x}\right) + \frac{2\pi}{\lambda}\left(f_4 - \sqrt{x^2 + y^2 + f_4^2}\right) - \frac{2\pi}{\Lambda}y \end{Bmatrix} \quad p,\ q = 1,\ 2,\ 3,\ \cdots \tag{4}$$

Here, it is clear that the proposed SMM has three superposed phase profiles, as shown in Figure 2a–d: a vortex phase $\varphi(x,y) = \exp(il_j\theta)$, where $l_j = 1$–4 denotes the topological charges of four OVs, the lens phases $\varphi_{j\_\mathrm{lens}} = \frac{2\pi}{\lambda}\left(f_j - \sqrt{x^2 + y^2 + f_j^2}\right)$, where we set $f_1 = 1600$ μm, $f_2 = 2000$ μm, $f_3 = 2400$ μm, and $f_4 = 2800$ μm, and the tilt phase φ_{tilt}, which can be determined by the period of supercell Λ. The introduction of the tilt phase along the x and y directions will induce a momentum shift in the corresponding direction, $\Delta k_x = -2\sigma_{\pm}(\pi/\Lambda)$ and $\Delta k_y = -2\sigma_{\pm}(\pi/\Lambda)$.[42] Consequently, as the beam propagates along the z axis, the real-space beam centroid undergoes a shift caused by the momentum shift, which can be described as

$$\begin{cases} \Delta x = \dfrac{\Delta k_x}{k_0} Z = -\sigma_{\pm}\dfrac{\partial \varphi_{\mathrm{tilt}}}{\partial x} = -\sigma_{\pm}\lambda Z/\Lambda \\ \Delta y = \dfrac{\Delta k_y}{k_0} Z = -\sigma_{\pm}\dfrac{\partial \varphi_{\mathrm{tilt}}}{\partial y} = -\sigma_{\pm}\lambda Z/\Lambda \end{cases} \tag{5}$$

To construct our metadevice, 8-phase levels from 0 to 2π with $1/4\pi$ step under CP normal incidence were chosen, which has determined that $\Lambda = 6.4$ μm is the supercell period along the phase gradient direction. Moreover, it should be noted that the real-space shift along the x and y directions can be different if the parameter Λ changes. As shown in Figure 2e, integral phase profiles of a mixed-phase distribution from four subareas are composed of 400 × 400 nanofins. Parts f–h of Figure 2 show images of the fabricated SMM using optical microscopy and scanning electron microscopy (SEM) of the fabricated TiO_2 nanofin array, which are consistent with the design. In the experiment, the entire area of the sample has increased to 200 × 200 μm^2, which is composed of 500 × 500 nanofins for verifying the performance of the proposed SMM.

https://doi.org/10.1021/acs.nanolett.5c02519
Nano Lett. 2025, 25, 14237–14245

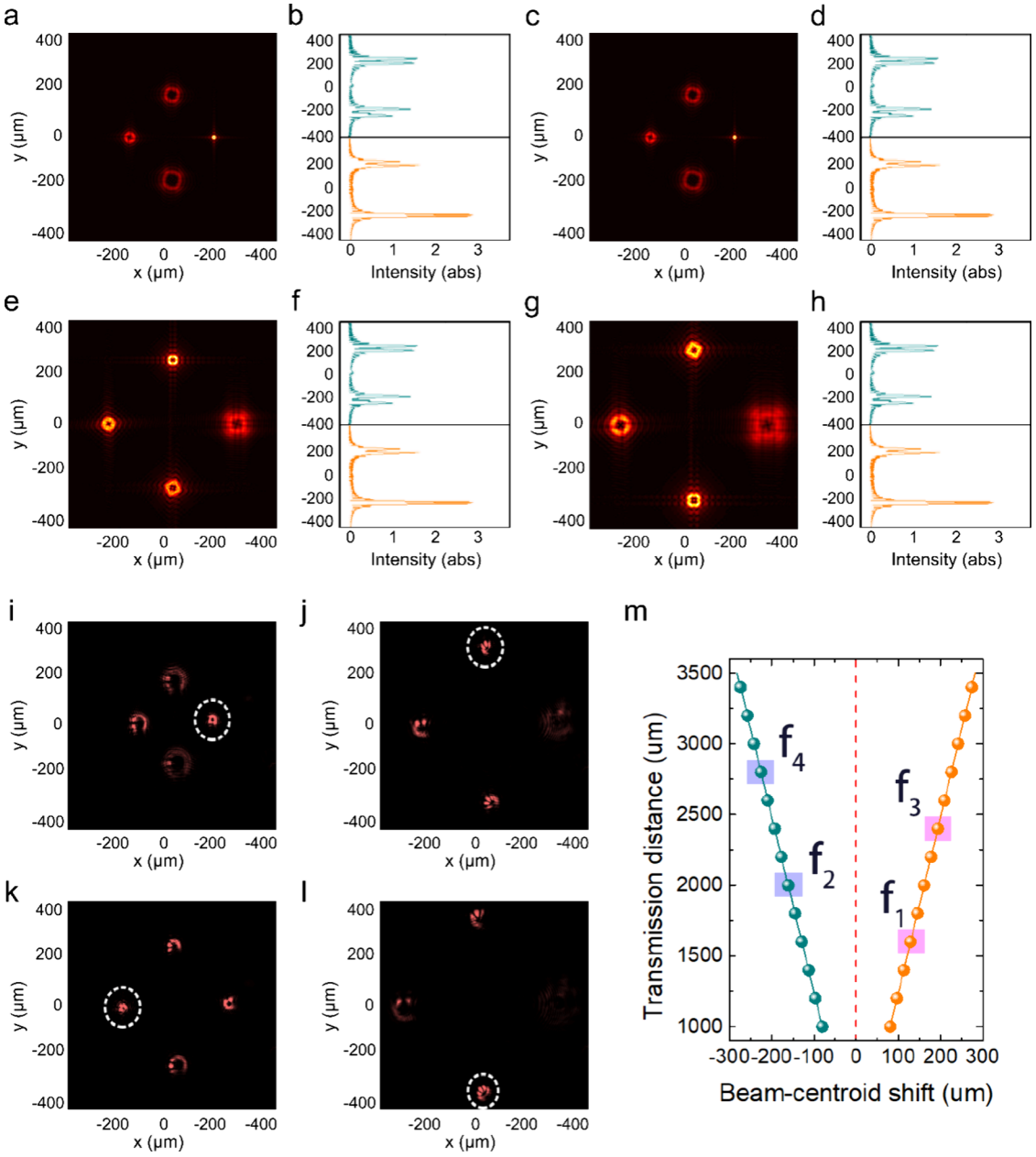

Figure 3. Off-axis spatial-variant OAMs with different topological charges generated by the proposed SMM. (a, c, e, and g) Theory-calculated results of the far-field intensity profiles with the four different focal planes for CP illumination. The corresponding far-field intensities along the green and orange dashed lines are shown in parts b, d, f, h, and i–l. The experimental results with different focal planes and the corresponding focus points are marked by circular dashed lines. (m) Calculated results for the beam-centroid shift versus transmission distance. The marked dots represent the exact different focal distances.

In principle, when a beam is incident on the SMM, the discrete Fraunhofer diffraction integral is employed to calculate the optical field $U_2(m_2,n_2)$ on the image plane from the optical field $U_1(m_1,n_1)$ on the source plane:

$$U_2(m_2, n_2) = \sum_{m_1=1}^{M} \sum_{n_1=1}^{N} G_x(m_2, m_1)\, U_1(m_2, n_1)\, G'_y(n_2, n_1) \tag{6}$$

where m_1, n_1 (m_2, n_2) are the subscripts of the discrete optical field matrix U_1 (U_2) and $M \times N$ is the size of U_1, which is 800 × 800 in our case. $G_x(m_2,m_1)$ and $G_y(n_2,n_1)$ are the discrete Fraunhofer transform matrixes, which can be described as

$$G_x(m_2, m_1) = \frac{e^{jkf}}{\sqrt{j\lambda f}} \exp\left(\frac{-jk}{f} m_2\delta_2 \cdot m_1\delta_1\right) \tag{7}$$

$$G_y(m_2, m_1) = \frac{e^{jkf}}{\sqrt{j\lambda f}} \exp\left(\frac{-jk}{f} n_2\delta_2 \cdot n_1\delta_1\right) \tag{8}$$

where f is the focal length of the Fourier lens and can be arbitrarily varied in the process of designing the SMM and δ_1 and δ_2 are the pixel sizes on the SMM plane and image plane, respectively. Four stable and high-quality OV beams can be generated after calculation, which are shown in parts a, c, e, and g of Figure 3, respectively. For verifying the phase profiles generated by the SMM, we have extracted the intensity

https://doi.org/10.1021/acs.nanolett.5c02519
Nano Lett. 2025, 25, 14237−14245

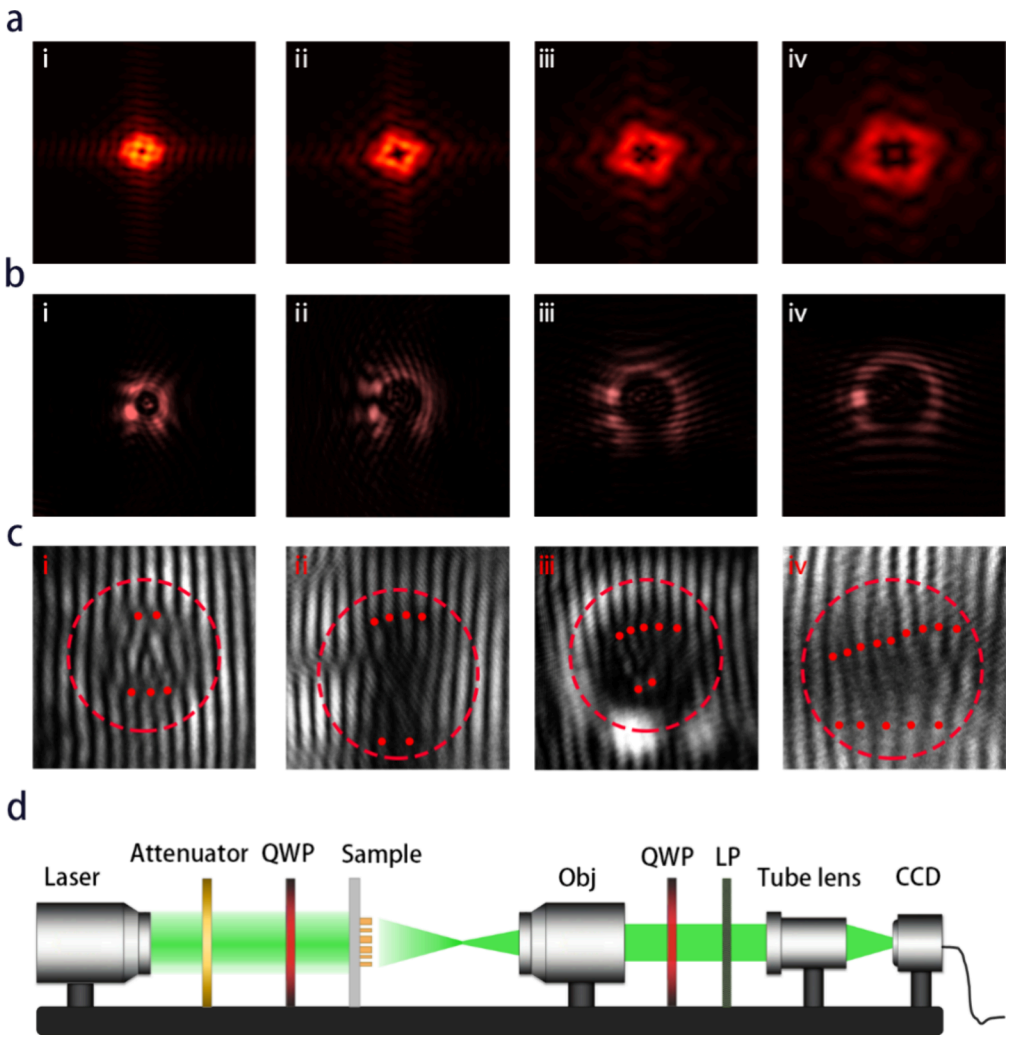

Figure 4. Measured intensity profiles and corresponding interference patterns of the off-axis multichannel OV lens. (a) Theory-calculated four magnified focal points. (b) Corresponding experimental four magnified focal points. (c) Interference patterns of the beam's $x-y$ cross sections at the four focal planes. The places where the forks appear have been marked by red circular dashed lines. (d) Optical measurement setup for the metasurface, consisting of a laser with the desired wavelength whose beam is passing through an attenuator and a quarter-waveplate (QWP) to generate the input light with the desired polarization to illuminate the metasurface. The far-field distributions of transmitted cross-polarized light are captured by a CCD camera.

distributions at the four focal planes when the SMM is illuminated by 514 nm LCP light. It is shown that the radius of the four focused OVs become larger and larger with the increase of the topological charges, which is caused by the positive proportional relationship between the focal lengths and the topological charges. There is no doubt that the intensity distribution of the output field will diverge with the propagation of light, although it has been compressed by introducing the function of focus. Furthermore, critically, the different spin states acquire two mutually conjugated tilted phases due to introduction of the linearly gradient phase in the SMM, implying that the output beams will diverge in opposite directions when the spin state of the incident CP light is reversed. Similarly, the focal plane $f = \sigma_{\pm} f_j$ is spin-dependent, which can be regarded as a convex/concave lens under the illumination of LCP and RCP light. Parts d, f, and h of Figure 3 show the charge-coupled device (CCD)-recorded far-field intensity distributions along the green and orange dashed lines marked in Figure 3m, demonstrating that different OVs achieve maximum intensity on their corresponding focal planes. It can be observed that peaks, which decrease with increasing the transmission distance, exhibit a dip due to the unique doughnut-shaped far-field distribution of the OV. Parts i–l of Figure 3 show the corresponding intensity of the experimentally measured far-field distribution on the different focal planes, which are consistent with the calculated results. The reason why the far-field distribution does not form a closed doughnut shape is that the filtered system is not explicit enough in the optical measurements. In this manner, the stray light that causes interference with the target light field leads to distortion in the far-field. Interestingly, the beam-centroid shifts obtained by four generated OV beams are equal due to the same deflected angles, although the beam-centroid shifts varied by the transmitted distance. The deflected angle can be calculated by $\varphi_{\text{tilt}} = \arcsin(\lambda/\Lambda) = 4.6°$. In this way, combined with eq 5, the precise coordinates of the four focus points should be $(\sigma_{\pm}\lambda f_1/\Lambda, 0, f_1)$, $(-\sigma_{\pm}\lambda f_2/\Lambda, 0, f_2)$, $(0, \sigma_{\pm}\lambda f_3/\Lambda, f_3)$ and $(0, -\sigma_{\pm}\lambda f_4/\Lambda, f_4)$, which are (128.5 μm, 0 μm, 1600 μm), (−160.63 μm, 0 μm, 2000 μm), (0 μm, 192.75 μm, 2400 μm), and (0 μm, −224.88 μm, 2800 μm), respectively, in our

https://doi.org/10.1021/acs.nanolett.5c02519
Nano Lett. 2025, 25, 14237−14245

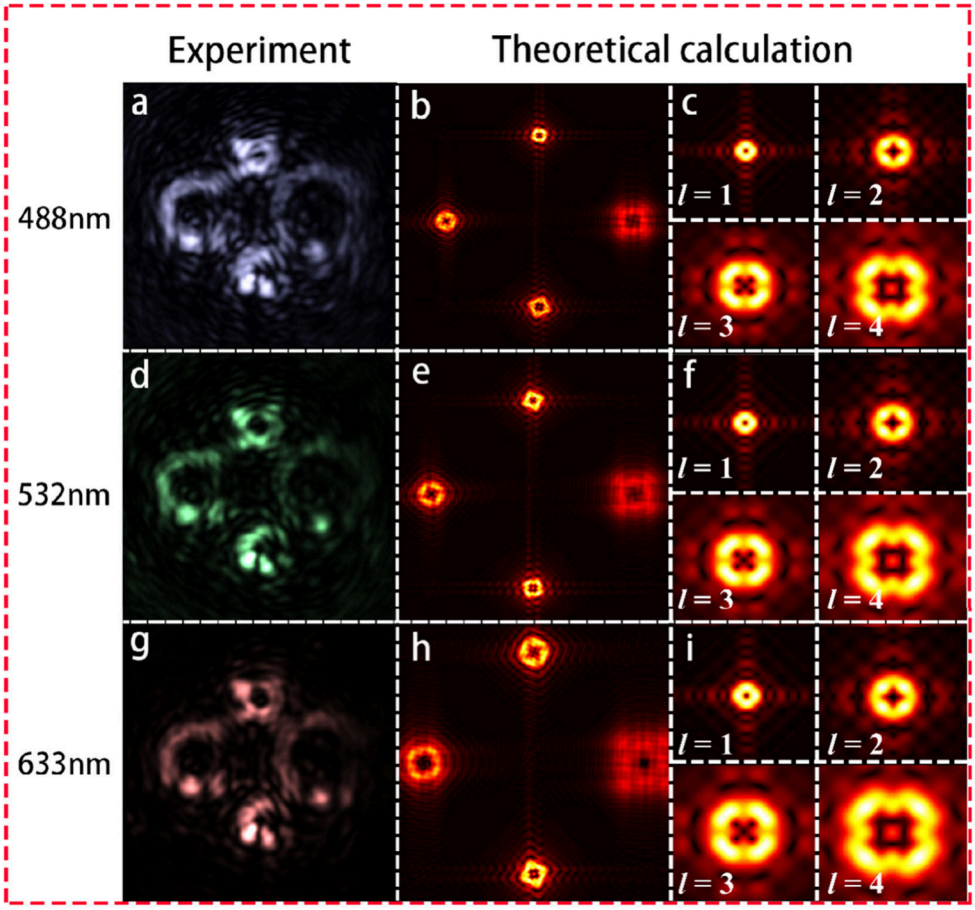

Figure 5. Properties of the broadband SMM. Measured intensity distributions of the output field in z = 3000 μm through the metadevice at wavelengths of (a) 488 nm, (d) 532 nm, and (g) 633 nm. (b, e, and h) Corresponding theory-calculated results in the same plane. The intensity of the output fields in the different focal planes at wavelengths of (c) 488 nm, (f) 532 nm, and (i) 633 nm, where subpanels sequentially correspond to vortex beams carrying topological charges l = 1−4 under CP illumination.

exemplary designs. Moreover, the beam-centroid shifts shown in Figure 3m are different from the calculated results, which is caused by the introduction of the scale factor η = 0.8 between the pixelated far-field distribution and calculated beam-centroid shifts in the process of a discrete Fraunhofer diffraction integral. For a demonstration of the flexible and independent manipulation among the different channels of the proposed SMM, the four beams generated by SMM with different deflected angles have also been investigated, as shown in Figure S3.

The magnified amplitude distributions of the individual off-axis OVs simulated on different focal planes are shown in Figure 4a, while the corresponding experimental results are shown in Figure 4b. As can be observed, the square-shaped modulation, distinct from the traditional doughnut-shaped distribution of OVs, is ascribed to the square shape of the structure. In order to clearly observe the profiles of the four OV beams, measurements were taken on four defocused planes, confirming that the area of the dark core of the OVs increases with increasing topological charge. Furthermore, to ascertain the topological charges of the OV beams, magnified interferometry patterns are presented in Figure 4c. Near the centers of the OV beams, the numbers of interfered fork-shaped fringe patterns, indicative of the topological charges of the OV beams, are 1, 2, 3, and 4, corresponding to the beam array design. The experimental setup for measuring the far-field intensity distributions of our proposed SMM is shown in Figure 4d, with detailed descriptions provided in the Materials and Methods section.

Furthermore, additional analyses and experiments to assess the broadband robustness of the proposed SMM, originating from the PB phase, were conducted. To confirm the broadband characteristics of the proposed SMM, it was subjected to illumination under different wavelengths of light. As depicted in Figure 5a,d,g, the experimental far-field distributions under different wavelength incidences were measured on a defocus plane (z = 3000 μm). The experimentally measured far-field distributions exhibited stability despite illumination by different wavelength incidences, indicating that the SMM can operate effectively in a broadband manner. Concurrently, to corroborate the experimental findings, the corresponding calculated far-field distributions are presented in Figure 5b,e,h. It is found that the distances between the four far-field spots and the center increase progressively with an increasing wavelength of incidence. Furthermore, each individual spot generated by its respective channel diverges progressively as the wavelength of incidence increases. Additionally, the brightness of the far-field spots intensifies with an increase in the topological charges of the OV beams, as evidenced by the measured focal plane being closest to f_4. The magnified far-field spots are depicted in Figure 5c,f,i, showcasing the profiles of the generated OV

https://doi.org/10.1021/acs.nanolett.5c02519
Nano Lett. 2025, 25, 14237−14245

beams with different topological charges on the four distinct focal planes. The broadband characteristics of the SMM are demonstrated by the similar profiles of individual spots generated by each channel under different wavelengths of illumination, albeit with an inevitable divergence due to dispersion. Simultaneously, the relative efficiency of the SMM under various wavelengths of incidence remains at a high level (refer to Figure S4).

In summary, we have theoretically and experimentally demonstrated spatial multiplexing of the OAM manipulation in both angular and distance domains. The proposed SMM with spatially variant oriented TiO_2 nanofins can divide an incident CP wave into four topologically charged beams in different directions and focus in four different planes in a broadband manner. Our metadevice builds a flexible connection between the OAM and the 3D spatial intensity distribution, which can be employed to further increase the information channel capacity. We believe that the ultracompact SMM with more unique extensibility and flexibility may inspire advanced photonic applications with versatile functionalities.

■ ASSOCIATED CONTENT

Supporting Information

The Supporting Information is available free of charge at https://pubs.acs.org/doi/10.1021/acs.nanolett.5c02519.

Supporting movie (AVI)

Measured optical constant of TiO_2 and the cross-polarized efficiency, broadband SMM design by optimization of the parameters, demonstration of the flexible design of deflected angles, broadband relative efficiency of the SMM, and materials and methods (PDF)

■ AUTHOR INFORMATION

Corresponding Authors

Yuancheng Fan − *School of Physical Science and Technology, Northwestern Polytechnical University, Xi'an 710129, China;* orcid.org/0000-0002-7919-4148; Email: phyfan@nwpu.edu.cn

Junjie Li − *Beijing National Laboratory for Condensed Matter Physics, Institute of Physics, Chinese Academy of Sciences, Beijing 100190, China; Songshan Lake Materials Laboratory, Dongguan, Guangdong 523808, China;* orcid.org/0000-0002-1508-9891; Email: jjli@iphy.ac.cn

Fuli Zhang − *School of Physical Science and Technology, Northwestern Polytechnical University, Xi'an 710129, China;* Email: fuli.zhang@nwpu.edu.cn

Authors

Wei Zhu − *School of Physical Science and Technology, Northwestern Polytechnical University, Xi'an 710129, China; Beijing National Laboratory for Condensed Matter Physics, Institute of Physics, Chinese Academy of Sciences, Beijing 100190, China; School of Microelectronics, Wuhan Textile University, Wuhan 430200, P. R. China*

Ruisheng Yang − *School of Physical Science and Technology, Northwestern Polytechnical University, Xi'an 710129, China*

Huan Zhao − *Department of Physics, Harbin Institute of Technology, Harbin 150001, China; Beijing Key Laboratory of Metamaterials and Devices, Key Laboratory of Terahertz Optoelectronics, Ministry of Education, Beijing Advanced Innovation Center for Imaging Theory and Technology, Department of Physics, Capital Normal University, Beijing 100048, China*

Guangzhou Geng − *Beijing National Laboratory for Condensed Matter Physics, Institute of Physics, Chinese Academy of Sciences, Beijing 100190, China*

Xuyue Guo − *School of Physical Science and Technology, Northwestern Polytechnical University, Xi'an 710129, China;* orcid.org/0000-0003-4152-1163

Peng Li − *School of Physical Science and Technology, Northwestern Polytechnical University, Xi'an 710129, China*

Quanhong Fu − *School of Physical Science and Technology, Northwestern Polytechnical University, Xi'an 710129, China*

Kangyao Sun − *School of Physical Science and Technology, Northwestern Polytechnical University, Xi'an 710129, China*

Changzhi Gu − *Beijing National Laboratory for Condensed Matter Physics, Institute of Physics, Chinese Academy of Sciences, Beijing 100190, China;* orcid.org/0000-0002-2689-2807

Yan Zhang − *Beijing Key Laboratory of Metamaterials and Devices, Key Laboratory of Terahertz Optoelectronics, Ministry of Education, Beijing Advanced Innovation Center for Imaging Theory and Technology, Department of Physics, Capital Normal University, Beijing 100048, China;* orcid.org/0000-0001-9235-6861

Complete contact information is available at: https://pubs.acs.org/10.1021/acs.nanolett.5c02519

Author Contributions

W.Z., Y.F., R.Y., H.Z., and Y.Z. carried out the device design and simulation. W.Z. and G.G. carried out the fabrication. X.G., Q.F., and P.L. carried out the measurements. All authors participated in analysis and discussion of the results. W.Z. and Y.F. wrote the manuscript with the help from others. J.L., F.Z., C.G., and Y.F. supervised the project.

Notes

The authors declare no competing financial interest.

■ ACKNOWLEDGMENTS

The work was supported by the National Key R&D Program of China (Grant 2023YFB3811400), the National Natural Science Foundation of China (Grants 12074314, 12304430, U21A20140, and 12074420), the Key Research Program of Frontier Sciences of CAS (Grant QYZDJ-SSW-SLH042), the Science and Technology New Star Program of Shaanxi Province (Grant 2023KJXX-148), the Beijing Municipal Science & Technology Commission, Administrative Commission of Zhongguancun Science Park (No. Z211100004821009), and the Fundamental Research Funds for the Central Universities.

■ REFERENCES

(1) Wu, Y.; Yang, W.; Fan, Y.; Song, Q.; Xiao, S. *Science Advances* **2019**, *5* (11), No. eaax0939.

(2) Einck, V. J.; Torfeh, M.; McClung, A.; Jung, D. E.; Mansouree, M.; Arbabi, A.; Watkins, J. J. *ACS Photonics* **2021**, *8* (8), 2400−2409.

(3) Khorasaninejad, M.; Chen, W. T.; Devlin, R. C.; Oh, J.; Zhu, A. Y.; Capasso, F. *Science* **2016**, *352* (6290), 1190−1194.

(4) Devlin, R. C.; Khorasaninejad, M.; Chen, W. T.; Oh, J.; Capasso, F. *Proc. Natl. Acad. Sci. U. S. A.* **2016**, *113* (38), 10473−10478.

(5) Liu, Y.; Qu, G.; Jiang, X.; Han, J.; Ji, Z.; Liu, Z.; Song, Q.; Yu, S.; Xiao, S. *Laser Photonics Review* **2023**, *17* (6), No. 2200712.

(6) Zhang, X.; Liu, Y.; Han, J.; Kivshar, Y.; Song, Q. *Science* **2022**, *377* (6611), 1215−1218.

(7) Wu, Y.; Wang, Y.; Yang, W.; Song, Q.; Chen, Q.; Qu, G.; Han, J.; Xiao, S. *Laser Photonics Review* **2021**, *15* (2), No. 2000330.
(8) Zhu, W.; Yang, R.; Geng, G.; Fan, Y.; Guo, X.; Li, P.; Fu, Q.; Zhang, F.; Gu, C.; Li, J. *Nanophotonics* **2020**, *9* (14), 4327−4335.
(9) Devlin, R. C.; Ambrosio, A.; Rubin, N. A.; Mueller, J. P. B.; Capasso, F. *Science* **2017**, *358* (6365), 896−901.
(10) Porfirev, A.; Khonina, S.; Kuchmizhak, A. *Progress in Quantum Electronics* **2023**, *88*, No. 100459.
(11) Allen, L.; Beijersbergen, M. W.; Spreeuw, R. J. C.; Woerdman, J. P. *Phys. Rev. A* **1992**, *45* (11), 8185−8189.
(12) Fang, Y.; Guo, Z.; Ge, P.; Dou, Y.; Deng, Y.; Gong, Q.; Liu, Y. *Light: Science Applications* **2022**, *11* (1), 34.
(13) Padgett, M.; Bowman, R. *Nat. Photonics* **2011**, *5* (6), 343−348.
(14) Leach, J.; Jack, B.; Romero, J.; Jha, A. K.; Yao, A. M.; Franke-Arnold, S.; Ireland, D. G.; Boyd, R. W.; Barnett, S. M.; Padgett, M. J. *Science* **2010**, *329* (5992), 662−665.
(15) Wang, M.; Chen, L.; Choi, D.-Y.; Huang, S.; Wang, Q.; Tu, C.; Cheng, H.; Tian, J.; Li, Y.; Chen, S.; Wang, H.-T. *Nano Lett.* **2023**, *23* (9), 3921−3928.
(16) Wu, H.; Yu, B.; Jiang, J.; Li, C.; RosalesGuzmán, C.; Liu, S.; Zhu, Z.; Shi, B. *Phys. Rev. Lett.* **2023**, *130* (15), No. 153803.
(17) Wang, J.; Yang, J.-Y.; Fazal, I. M.; Ahmed, N.; Yan, Y.; Huang, H.; Ren, Y.; Yue, Y.; Dolinar, S.; Tur, M.; Willner, A. E. *Nat. Photonics* **2012**, *6* (7), 488−496.
(18) Wang, J. *Photon. Res.* **2016**, *4* (5), B14−B28.
(19) Forbes, A.; Dudley, A.; McLaren, M. *Adv. Opt. Photon.* **2016**, *8* (2), 200−227.
(20) Qu, K.; Jia, Q.; Fisch, N. J. *Phys. Rev. E* **2017**, *96* (5), No. 053207.
(21) Curtis, J. E.; Grier, D. G. *Phys. Rev. Lett.* **2003**, *90* (13), No. 133901.
(22) Khonina, S. N.; Ustinov, A. V.; Logachev, V. I.; Porfirev, A. P. *Phys. Rev. A* **2020**, *101* (4), No. 043829.
(23) Passier, R.; Devaux, F.; Chauvet, M. *Opt. Express* **2008**, *16* (10), 7134−7141.
(24) Ruffato, G.; Rossi, R.; Massari, M.; Mafakheri, E.; Capaldo, P.; Romanato, F. *Sci. Rep.* **2017**, *7* (1), No. 18011.
(25) Yu, N.; Genevet, P.; Kats, M. A.; Aieta, F.; Tetienne, J.-P.; Capasso, F.; Gaburro, Z. *Science* **2011**, *334* (6054), 333−337.
(26) Karimi, E.; Schulz, S. A.; De Leon, I.; Qassim, H.; Upham, J.; Boyd, R. W. *Light Science & Applications* **2014**, *3* (5), e167−e167.
(27) Yuan, Y.; Zhang, K.; Ratni, B.; Song, Q.; Ding, X.; Wu, Q.; Burokur, S. N.; Genevet, P. *Nat. Commun.* **2020**, *11* (1), 4186.
(28) Mei, S.; Mehmood, M. Q.; Hussain, S.; Huang, K.; Ling, X.; Siew, S. Y.; Liu, H.; Teng, J.; Danner, A.; Qiu, C.-W. *Adv. Funct. Mater.* **2016**, *26* (29), 5255−5262.
(29) Zhang, Y.; Liu, W.; Gao, J.; Yang, X. *Advanced Optical Materials* **2018**, *6* (4), No. 1701228.
(30) Choudhury, S. M.; Wang, D.; Chaudhuri, K.; DeVault, C.; Kildishev, A. V.; Boltasseva, A.; Shalaev, V. M. *Nanophotonics* **2018**, *7* (6), 959−987.
(31) Jeong, J.; Goldflam, M. D.; Campione, S.; Briscoe, J. L.; Vabishchevich, P. P.; Nogan, J.; Sinclair, M. B.; Luk, T. S.; Brener, I. *ACS Photonics* **2020**, *7* (7), 1699−1707.
(32) Gu, J.; Liu, Y.; Meng, N.; Sahmuganathan, V.; Tan, S. C.; Sudijono, J.; Tang, J.; Venkatasubramanian, E.; Mallick, A.; Tjiptoharson, F.; Rezaei, S. D.; Teo, S. L.; Zhu, Q.; Chen, Y.; Lin, M.; Dong, Z.; Loh, K. P. *Advanced Optical Materials* **2023**, *11* (6), No. 2202826.
(33) Yang, B.; Liu, W.; Li, Z.; Cheng, H.; Choi, D.-Y.; Chen, S.; Tian, J. *Nano Lett.* **2019**, *19* (7), 4221−4228.
(34) Chong, K. E.; Staude, I.; James, A.; Dominguez, J.; Liu, S.; Campione, S.; Subramania, G. S.; Luk, T. S.; Decker, M.; Neshev, D. N.; Brener, I.; Kivshar, Y. S. *Nano Lett.* **2015**, *15* (8), 5369−5374.
(35) Maguid, E.; Yulevich, I.; Veksler, D.; Kleiner, V.; Brongersma, M. L.; Hasman, E. *Science* **2016**, *352* (6290), 1202−1206.
(36) Fang, X.; Ren, H.; Gu, M. *Nat. Photonics* **2020**, *14* (2), 102−108.
(37) Ren, H.; Fang, X.; Jang, J.; Bürger, J.; Rho, J.; Maier, S. A. *Nat. Nanotechnol.* **2020**, *15* (11), 948−955.
(38) Jin, Z.; Janoschka, D.; Deng, J.; Ge, L.; Dreher, P.; Frank, B.; Hu, G.; Ni, J.; Yang, Y.; Li, J.; Yu, C.; Lei, D.; Li, G.; Xiao, S.; Mei, S.; Giessen, H.; zu Heringdorf, F. M.; Qiu, C.-W. *eLight* **2021**, *1* (1), 5.
(39) Wang, M.; Hu, G.; Chand, S.; Cotrufo, M.; Abate, Y.; Watanabe, K.; Taniguchi, T.; Grosso, G.; Qiu, C.-W.; Alù, A. *eLight* **2022**, *2* (1), 12.
(40) Wang, X.; Wang, H.; Wang, J.; Liu, X.; Hao, H.; Tan, Y. S.; Zhang, Y.; Zhang, H.; Ding, X.; Zhao, W.; Wang, Y.; Lu, Z.; Liu, J.; Yang, J. K. W.; Tan, J.; Li, H.; Qiu, C.-W.; Hu, G.; Ding, X. *Nat. Commun.* **2023**, *14* (1), 2063.
(41) Deng, M.; Kanwal, S.; Wang, Z.; Cai, C.; Cheng, Y.; Guan, J.; Hu, G.; Wang, J.; Wen, J.; Chen, L. *Nano Lett.* **2024**, *24* (46), 14641−14647.
(42) Shitrit, N.; Bretner, I.; Gorodetski, Y.; Kleiner, V.; Hasman, E. *Nano Lett.* **2011**, *11* (5), 2038−2042.

https://doi.org/10.1021/acs.nanolett.5c02519
Nano Lett. 2025, 25, 14237−14245